Mesh-moving arbitrary Lagrangian-Eulerian three-dimensional technique applied to sloshing problems

Laura Battaglia[a,b,*], Ezequiel López[c], Marcela Cruchaga[d], Mario Storti[a], Jorge D'Elía[a]

[a] *Centro de Investigación de Métodos Computacionales (CIMEC), UNL-CONICET, Predio CONICET Santa Fe "Dr. Alberto Cassano", Colectora Ruta Nac. Nro 168, Km 0, Paraje El Pozo, Santa Fe, Argentina*

[b] *Grupo de Investigación de Métodos Numéricos en Ingeniería (GIMNI), Univ. Tecnológica Nacional, Facultad Regional Santa Fe, Lavaise 610, Santa Fe, Argentina*

[c] *Instituto de Investigación en Tecnologías y Ciencias de la Ingeniería (IITCI), UNCOMA/CONICET, Buenos Aires 1400, 8300 Neuquén, Argentina*

[d] *Departamento de Ingeniería Mecánica, Universidad de Santiago de Chile (USACH). Av. Bdo. O'Higgins 3363, Santiago de Chile, Chile*

Abstract

Validation of three-dimensional (3D) sloshing models is a relevant task in order to guarantee the correctness of numerical predictions. In this work, attention is focused on assessing the 3D free surface (FS) evolution when an Arbitrary Lagrangian-Eulerian method is applied to solve sloshing problems. The computational scheme consists of three stages: (i) solve the incompressible Navier-Stokes equations over a single fluid domain with a FS; (ii) determine the FS displacements from the velocity field computed at (i); and (iii) update the mesh with a computational mesh dynamic problem. The study aims to evaluate the global mass-conservation strategy reported in this work for long term simulations. The forced sloshing cases present moderate FS displacements with complex wave pattern behaviours. Specifically, sloshing in a tank with a stepped shape in the bottom and two sloshing cases of a rectangular tank are presented. The numerical results are compared with experimental data to evaluate the performance of the proposed model.

*Corresponding Author

Email address: lbattaglia@santafe-conicet.gov.ar (Laura Battaglia)

Keywords: fluid mechanics, free surface, arbitrary Lagrangian-Eulerian method, sloshing, computational mesh dynamics

1. Introduction

Free Surface (FS) flows are typical problems in fluid mechanics, as well as in engineering applications, such as ship hydrodynamics [1], open channel flows [2], and sloshing in tanks [3, 4, 5]. As a consequence, several numerical methods were developed to predict FS displacements, as well as the behaviour of the liquid beneath or around that particular interface.

Different approaches have been developed to solve sloshing problems. Analytical solutions are found in the literature assuming incompressible and irrotational flows. In such a case, potential flow theory can be used to solve the governing equations where the free surface is described using low-order asymptotic [6] and multimodal [7] methods. These techniques have been applied to study the sloshing in tanks with different shapes and filling levels [8, 9].

In recent decades, many efforts have been devoted to computationally model the fluid dynamics including interfaces between fluids and free surfaces [10]. Several numerical methods have been developed to particularly address long-term free surface analysis in the framework of different discretization schemes, i.e., finite difference, finite volume, finite element, meshfree and boundary elements formulations. A short but not exhaustive list of works illustrating different kinds of techniques developed to describe free surface flows is as follows: the volume of fluid (VOF) [11, 12, 13, 14, 15], level set (LS) [16, 17, 18], Eulerian-Lagrangian [19, 20], deforming domain [21, 22], smooth particle hydrodynamics [23, 24, 25, 26], particle finite element [27], and boundary elements [5]. To improve the performance of the methods, the above techniques have been coupled, resulting in hybrid or mixed formulations, e.g., mixed LS and VOF methods [28, 29] or the particle level set method [30], and others [31, 32].

These works describe fixed-mesh as well as moving-mesh techniques [33]. In general, in the fixed-mesh methods, the numerical domain involves the liquid and the gaseous phase, represented with a fixed discretization, while the interface is determined in a particular way depending on the applied technique. These methods allow the resolution of problems with interface breaking or folding and with large displacements. The moving-mesh methods

are proposed in such a way that the interface, which constitutes a boundary of the numerical domain, is explicitly modelled with certain entities, i.e., nodes or faces of elements, as in Arbitrary Lagrangian-Eulerian (ALE) methods [34, 19], where the domain generally consists of a single fluid phase and its shape changes in time due to the FS displacements. These methods have been extensively used for solving sloshing problems, with the contributions of [35, 36] and [37] as recent examples. This kind of ALE technique has the advantage to analyze one single fluid domain preserving the sharp description of the interface. In contrast, the LS technique is a two fluid flow domain technique and requires an additional variable to track the interface.

Currently, the validation of the proposed models is an important task in order to guarantee accurate and predictive simulations. To this end, efforts have been made to contrast the numerical results with experimental data [13, 22, 20, 14, 38, 25, 26].

In the present work, a previously reported ALE technique [39] is improved with a mass-preserving algorithm blackfor long term simulations, as well as the transport of the interface is now solved with a stabilized method for 3D cases. In contrast with the cases reported in [39], the present formulation allows to solve sloshing cases with lower fluid viscosity. The mesh motion is modelled using a particular Computational Mesh Dynamics (CMD) technique. This technique, presented by López et al. [40], and initially developed for moving interfaces without shape change, is novelly applied to FS fluid flows. The developments are programmed in the in-house code PETSc-FEM [41], which is based on finite element libraries developed for parallel computing using the Message Passing Interface [42] and the Portable Extensible Toolkit for Scientific Computation (PETSc) libraries [43]. The proposed tool is applied to model three three-dimensional (3D) forced sloshing tests. The first test is the sloshing of a tank with a stepped-shape bottom. This case generates very complex wave patterns that are a challenge to model and to contrast the results with experimental data. The second and the third tests are moderate-amplitude cases in a rectangular tank shaken with two different oscillating frequencies; the predictions are also validated with experimental data.

The distinctive aspects of the work are summarized as follows:

- 3D one-phase mass-preserving stabilized ALE technique.
- mesh dynamics based on minimal distortion principle is extended to free surfaces general motion on a boundary.

- report of the sloshing in a tank with a stepped-shape bottom.
- experimental validation of the model.

The work is organized as follows. In Section 2, the governing equations are presented, as well as the numerical methods adopted for solving each stage. Section 3 describes experimental and numerical studies for the tank with stepped-bottom geometry and harmonic horizontal excitation. Section 4 is devoted to the numerical solution of a harmonically excited rectangular tank with moderate free surface displacements, where the performance of the mass conserving stage and mesh convergence are analysed. Finally, Section 5 summarizes the conclusions of the work.

2. Governing Equations

The FS flows solved by the proposed ALE strategy require the solution of three problems in each time step. The first one consists in solving the Navier-Stokes (NS) equations with a Finite Element Method (FEM). The second problem provides the displacements of the FS nodes according to the velocities from the NS solver, solving a transport problem with FEM and including a volume control strategy. Finally, the domain mesh is modified by a CMD model to account for the FS displacements.

2.1. Navier-Stokes equations

The ALE form of the NS equations solved over a fluid domain Ω in time $t \in (0, T]$ can be written as

$$\rho\left(\partial_t \boldsymbol{u} + \boldsymbol{c} \cdot \nabla \boldsymbol{u} - \boldsymbol{f}\right) - \nabla \cdot \boldsymbol{\sigma} = 0 \ ; \tag{1}$$

$$\nabla \cdot \boldsymbol{u} = 0 \ ; \tag{2}$$

where $\boldsymbol{u}$ is the fluid velocity, $\boldsymbol{f}$ is the body force, and ρ is the fluid density. The convective velocity $\boldsymbol{c}$ is defined as $\boldsymbol{c} = \boldsymbol{u} - \hat{\boldsymbol{u}}$, where the mesh velocity is $\hat{\boldsymbol{u}}$. The fluid stress tensor $\boldsymbol{\sigma} = \boldsymbol{\sigma}(\boldsymbol{u}, p)$ is

$$\boldsymbol{\sigma} = -p\mathbf{I} + \mathbf{T} \ ; \tag{3}$$

where in the isotropic term p is the pressure and $\mathbf{I}$ the identity tensor. Furthermore, the deviatoric term is $\mathbf{T} = 2\mu\boldsymbol{\varepsilon}$, i.e., it is linearly related to the strain rate $\boldsymbol{\varepsilon} = \boldsymbol{\varepsilon}(\boldsymbol{u}) = \frac{1}{2}(\nabla \boldsymbol{u} + \nabla^T \boldsymbol{u})$, being μ the fluid dynamic viscosity.

The boundary conditions are given by

$$\mathbf{u} = \mathbf{u}_{\mathrm{D}} \qquad \text{on } \Gamma_{\mathrm{D}}; \tag{4}$$

$$\boldsymbol{\sigma} \cdot \mathbf{n} = \mathbf{t} \qquad \text{on } \Gamma_{\mathbf{t}}; \tag{5}$$

with Γ_{D} the Dirichlet contour, as in solid walls, and $\Gamma_{\mathbf{t}}$ the traction contour, such that $\Gamma = \Gamma_{\mathrm{D}} \cup \Gamma_{\mathbf{t}}$ and $\Gamma_{\mathrm{D}} \cap \Gamma_{\mathbf{t}} = \emptyset$. The contour $\Gamma_{\mathbf{t}}$ constitute the interface between fluids, representing here the FS, Γ_{FS}, where the equilibrium condition is written as

$$\boldsymbol{\sigma}_l \cdot \mathbf{n} = \boldsymbol{\sigma}_g \cdot \mathbf{n} \qquad \text{on } \Gamma_{\mathrm{FS}}. \tag{6}$$

where the liquid and the gas stress tensors are $\boldsymbol{\sigma}_l$ and $\boldsymbol{\sigma}_g$, respectively, and $\mathbf{n}$ is the FS normal vector.

Assuming negligible viscosity and density for the gas, $\mathbf{T} \cdot \mathbf{n} = \mathbf{0}$ and $p = P_{\mathrm{atm}}$ on Γ_{FS}. Then, the traction forces are $\mathbf{t} = -P_{\mathrm{atm}}\ \mathbf{n}$ over the FS, where P_{atm} is the atmospheric pressure.

Viscous dissipation is taken into account with a simple turbulence model that consists of replacing μ by a simple algebraic model to represent the turbulent viscosity $\mu_t = \min(\mu + l_{\mathrm{mix}}^2 \rho \sqrt{2\boldsymbol{\varepsilon} : \boldsymbol{\varepsilon}}, \mu_{\max})$, given a mixing length l_{mix} and a cutoff value $\mu_{\max}$. The cutoff value is set in $\mu_{\max} = 0.1$ kg (m s)$^{-1}$ for water, while the mixing length can be estimated as $l_{\mathrm{mix}} = C_{\mathrm{t}}\ h$. In the present ALE method, and due to the mesh deformation, the elemental mixing length would change with mesh size during the analysis. Then, a fixed value is adopted, considering a mean h value in the non-deformed mesh and a typical value for C_{t} close to 0.18, taking the Smagorinsky turbulence parameter as a reference [44]. Based on our previous experience using level set type techniques in fixed mesh finite element analyses, this approach helps to stabilize the solution at the shear boundary on the free surface. Besides, the cutoff viscosity avoids excessive dissipation when large l_{mix} values are assigned. This aspect is also present in the one-phase ALE analysis for free surface flow problems. This model was previously applied to sloshing analyses, see [45, 33, 20] and references therein, as well as similar ones are reported in the literature [46, 47, 29].

The PETSc-FEM [41] NS solver with streamline upwind/Petrov-Galerkin (SUPG) [48] and pressure stabilizing/Petrov-Galerkin (PSPG) [49] stabilizations is chosen to solve Eqs. (1,2). The time integration is performed using a θ-method, typically with $\theta = 0.55$. The convergence order for the present ALE-FEM approximation is $(O)(h^2)$, as reported in [39].

2.2. Free surface displacements

The displacement of each node j of the interface is measured over a fixed direction of unit vector $\hat{\boldsymbol{s}}_j$, giving the node position $\boldsymbol{x}_j$ in time t as in [39]

$$\boldsymbol{x}_j(t) = \boldsymbol{x}_{0,j} + \eta_j(t)\ \hat{\boldsymbol{s}}_j\ ; \tag{7}$$

where the initial position of the node is $\boldsymbol{x}_{0,j}$, and η_j is a scalar magnitude representing the nodal displacement along $\hat{\boldsymbol{s}}_j$, see Fig. 1(a). Note that the displacement directions given by $\hat{\boldsymbol{s}}_j$ are provided only for the nodes of the FS, and are chosen normal to the interface at rest, particularly the x_3-coordinate in the examples to be shown. Then, the free surface represented is single-valued, i.e. only one interface position is given for each $\hat{\boldsymbol{s}}_j$, in such a way it is not possible to represent folding or detachment of the fluid.

The kinematic FS condition is applied to determine the scalar coordinate η,

$$\boldsymbol{u}\cdot\boldsymbol{n} = \partial_t\boldsymbol{\eta}\cdot\boldsymbol{n} \quad \text{over } \Gamma_{\mathrm{FS}}; \tag{8}$$

where $\boldsymbol{\eta} = \eta\ \hat{\boldsymbol{s}}$, giving

$$\partial_t\eta = \frac{\boldsymbol{u}\cdot\boldsymbol{n}}{\hat{\boldsymbol{s}}\cdot\boldsymbol{n}}\ . \tag{9}$$

From here, the problem to be solved is

$$\partial_t\eta + \boldsymbol{u}_{\parallel}\cdot\hat{\nabla}\eta = s \qquad \text{in } \Gamma_{\mathrm{FS}} \tag{10}$$

where $\eta = \eta_{\mathrm{D}}$ over Γ'_{D}, and the velocity normal to the reference direction is $\boldsymbol{u}_{\parallel} = \frac{1}{\hat{\boldsymbol{s}}\cdot\boldsymbol{n}}\ [u_1;\quad u_2]^T$, while

$$\hat{\nabla}\eta = \left[\frac{\partial\eta}{\partial x_1};\quad \frac{\partial\eta}{\partial x_2}\right]^T; \tag{11}$$

and $s = u_3/(\hat{\boldsymbol{s}}\cdot\boldsymbol{n})$ is the source term given by the fluid velocity in the x_3 direction. Furthermore, Γ_{FS} in Eq. (8) is the $(n_{\mathrm{dim}}-1)$-dimension domain representing the FS and corresponding to a n_{dim} domain for the fluid flow Ω, as shown in Fig. 1(b). Dirichlet boundary conditions for the hyperbolic problem represented by Eq. (10) could be given on a boundary of the FS.

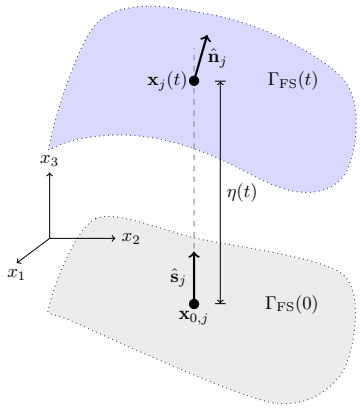

(a)

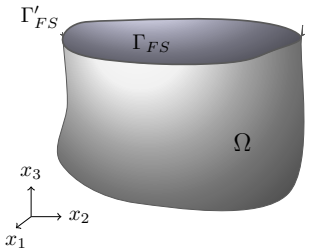

(b)

Figure 1: Domains and contours for ALE formulation (a) and free surface nodal displacements notation (b).

2.3. Mass-conserving strategy

The numerical loss of mass is a well-known fact to be considered in algorithms proposed to describe free surfaces and moving interfaces problems. Different mass preserving strategies have been proposed in the literature according to the used discretization scheme, see [33]. Some of these schemes require the definition of external user-defined parameters, while others are automatically set [50, 51]. The first scope of all formulations is to correctly reproduce experimental or numerical free surface evolution taken as reference to validate the models.

Here, a mass-conserving global scheme is applied to maintain the initial

volume of the domain, particularly for long-time simulations, which is analogous to that introduced in [45] for a LS method. The approach consists in correcting the elevation η_j^0 for each FS node over the node j at time t, as follows:

$$\eta_j(t) = \eta_j^0(t) + C_{\text{vol}}\ D_{\text{vol}}(V_n - V_0) \tag{12}$$

where $\eta_j(t)$ is the corrected FS elevation, C_{vol} is a dimensionless correcting coefficient, D_{vol} is the horizontal projection of the interface, V_n is the current total volume, and V_0 is the initial total volume. As the numerical scheme is explicit, $C_{\text{vol}} < 0.5$ has to be adopted to avoid numerical instabilities. In particular, the range $[0.05, 0.1]$ has been tested, giving satisfactory mass conserving results without appreciable differences in the solution for any case. The present strategy guarantees that the mass is globally preserved. In cases where the interface is highly distorted or split, cases not considered in the present overall free surface method, local mass conserving algorithms should be considered.

The SUPG stabilization [48] is applied to solve Eq. (10), using the advection-diffusion solver of the PETSc-FEM code, in which numerical diffusivity can be activated in the case that numerical instabilities appear. The time integration for such equations is also performed using a θ-method, with $\theta = 0.7$ for the examples shown here. The elevation field is updated each time step, requiring the velocity field $\boldsymbol{u}_{\|}$ for the nodes placed over the free surface, and the source term s. Next, the mass-conserving strategy corrects η with Eq. (12) and sends the current field to the mesh-moving instance as an imposed displacement.

2.4. Mesh movement

Once the FS nodal displacements are computed, as detailed in Sec. 2.2, the position of the mesh internal nodes have to be determined. To this purpose, there are typical alternatives to account for the deformation of the domain boundaries, reported in the literature. The most expensive choice is the remeshing of the domain, which also introduces errors due to the interpolation of nodal values from the old to the new mesh, in each time step or periodically during a simulation. Other authors perform an algebraic mesh update, limited to small FS displacements and structured meshes, see e.g. [52]. Another alternative consists of solving an auxiliary problem, such as a pseudo-elastic problem [53, 35, 54], a Laplace problem [36], or minimizing the elemental distortion of the mesh [40].

The present ALE method is prepared to work with the last alternative, i.e., solving an auxiliary problem for updating the internal nodal positions. For the moderate FS displacements of interest, the CMD proposed by López et al. [40] is chosen, which is based on the minimization of a global functional representing the distortion of the mesh defined as

$$F(\mathbf{x}) = \sum_e F_e(\mathbf{x}), \quad \text{with } F_e(\mathbf{x}) = 1/q_e^n \tag{13}$$

where the sum extends to all elements in the mesh, q_e is an element quality indicator, and $n \in \mathbb{N}$. As $n \to \infty$, the mesh distortion tends to the distortion of the 'worst' element in the mesh. In particular, the element quality indicator considered here is a geometrical indicator defined for simplicial elements (triangles in 2D and tetrahedra in 3D) as

$$q_e = C_{\mathrm{q}} \frac{V_e}{\sum_j l_{e,j}^{n_{\mathrm{dim}}}} \tag{14}$$

where $l_{e,j}$ is the length of the $j-$edge of the element, V_e is the element volume, $C_{\mathrm{q}} = 4\sqrt{3}$ for triangles and $C_{\mathrm{q}} = 36\sqrt{2}$ for tetrahedra. The value of the normalization constant C_{q} indicates that the equilateral simplicial element represents the optimal shape. For non-simplicial elements, the strategy is applied through the decomposition of the element into simplices. A drawback with this strategy occurs when the quality indicator tends to zero, since in such a case, the functional tends to infinity. This means that, e.g., the method does not work with a tangled mesh. According to Eq. (14), $q_e \to 0$ when $V_e \to 0$ and $\sum_j l_{e,j}^{n_{\mathrm{dim}}}$ is bounded below (i.e., the simplex is not collapsed to a single point). Therefore, the functional is regularized by replacing V_e in Eq. (14) by the following positive and strictly increasing function:

$$h(V_e) = \frac{V_e + \sqrt{V_e^2 + 4\delta^2}}{2} \tag{15}$$

where the parameter δ represents the value of the function when $V_e = 0$. For $\delta > 0$, the singularity in the functional is removed, and as $\delta \to 0$, $h(V_e) \to V_e$ for $V_e > 0$. Hence, an untangling mesh strategy is achieved by defining a decreasing sequence for the values of δ such that $\delta \to 0$ when the iteration number tends to infinity. Details of the mesh untangling and smoothing algorithm are presented in [55].

The sloshing problems considered in this work present moderate FS displacements, for which the CMD strategy based on the minimization of the element distortions is utilized. This CMD strategy was previously applied to the resolution of fluid-structure interaction problems, where some portion of the fluid domain boundary represents the interface with either a rigid or deformable solid. Hence, the application to free surface problems represents a challenge for the CMD strategy since the deformable boundary is governed now by the equations of fluid motion. Some features of the FS could be the presence of surface waves, high values or rapid changes in curvature, among others. These features represent local deformations to which the CMD strategy must accommodate to the mesh nodes to obtain a valid mesh. In limiting cases, when the interface tends to fold or break, and regarding that free surface nodes move only in x_3 direction, there may not be a valid mesh to fit the new shape of the domain, and the mesh movement stage does not converge. In these cases, the method fails instead of providing unphysical results. In the following, the robustness of the proposed CMD strategy is tested in sloshing cases with complex wave patterns and high FS elevations in comparison with the depth of the water.

At every time step, the mesh movement is solved as an steady case, considering the free-surface position with respect to the reference configuration, i.e., the initial mesh. Hence, the mesh movement at each time step is independent of previous time steps.

3. Forced sloshing of a tank with a stepped-shape bottom

3.1. Experimental work

A forced sloshing experiment in a tank with a stepped-shape bottom is proposed to evaluate the depth change effect on the wave pattern. The tank geometry and experimental set-up are shown in Fig. 2. The free surface evolution is captured using ultrasonic sensors located at certain points: sensor 1 at the middle of the shallow region, sensor 2 on the step and sensor 3 at the middle of the deeper part, as sketched in Fig. 2 (top). The experiments are also recorded using a high-speed camera at 120 frames per second. From such videos, the free surface is evaluated using image capturing techniques, with an error of ± 0.5 mm for the free surface position, which is of the same order as the error for ultrasonic sensors. The free surface history obtained from sensors and videos are compared and used to assess the repeatability and the

reliability of the experiments. The experimental technique was developed and applied to other sloshing problems, e.g, [20, 33, 45, 56, 57].

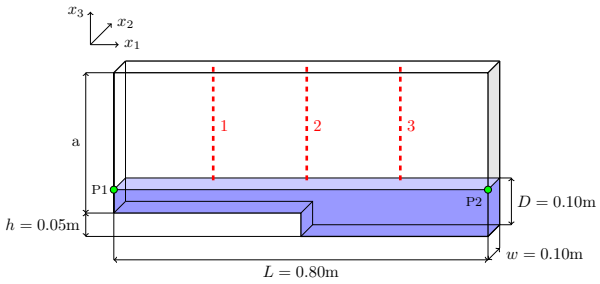

(a)

(b)

Figure 2: Tank geometry with sensor positions (1 to 3) and pressure numerical gauges (P1 and P2) (a). Experimental set-up (b) for the stepped-bottom tank.

The experimental data (obtained from a set of five test to warrant repeatability within experimental error) are reported with the numerical results in Section 3.2.

3.2. Simulation

As a single-phase strategy is used, only the volume occupied by the fluid (water) is considered the domain, with the sizes given in Fig. 2(top) and $w = 0.025$ m instead of 0.10 m in the real tank. Due to no experimental evidence of 3D effects along the width of the tank has been observed, we can define that the results do not present strong dependence on w; hence, the simulations are made using a reduced w for saving computational time. The reference mesh is generated with 26540 linear tetrahedral elements of maximum size $h_e = 8$ mm.

Perfect slip boundary conditions are imposed on the lateral walls to solve the Navier-Stokes equations, i.e., $\mathbf{u} \cdot \mathbf{n} = \mathbf{0}$, while bottom and step velocities are null, i.e., $\mathbf{u} = \mathbf{0}$. The dynamics of the mesh is solved with imposed displacements on the FS, and with perfect slip conditions over walls and at the bottom of the tank. As there are no entrances or exits of the fluid, the FS advection problem has no boundary conditions to impose.

The movement of the system is induced by a horizontal acceleration in x_1-direction with an amplitude of 7.5 mm and frequency $f = 0.45$ Hz. The vertical gravitational acceleration is $g = -9.81$ m s^{-2} in the x_3 direction.

The water properties are dynamic viscosity $\mu = 0.001$ kg (m s)$^{-1}$ and density $\rho = 998.2$ kg m^{-3}. For the turbulence model, a mixing length $l_{\text{mix}} = 0.75$ mm and a cutoff value for the turbulent viscosity of $\mu_{\text{max}} = 0.1$ kg (m s)$^{-1}$ are adopted.

The simulations were carried out with a time step $\Delta t = 0.005$ s, with a final time of $T_f = 150$ s. Initial conditions correspond to the tank at rest, i.e., with horizontal FS and null velocities in the whole domain. For the volume-preserving strategy, the correcting coefficient was set in $C_{\text{vol}} = 0.05$.

The amplitude of the displacements η of the free surface in the three sensor positions are plotted in Fig. 3. The displacements at sensor 1 and sensor 3 positions show higher amplitudes than those measured by sensor 2. The registers show several peaks for every period T of the table movement, from the effect of the bottom step placed in the middle of the tank, where some vortices are shed. The free surface displacements show phase regularity; however, the patterns are not uniform in amplitude, neither in the experimental results nor in the numerical results.

In Fig. 4, the numerical results are compared with the ultrasonic sensor register and image post-processing from the experiment. Furthermore, the table displacements are shown for the numerical tests and the image post-processing. The signals of sensors 1 and 3 are both well reproduced by the numerical approach, mostly regarding the phase of the movements, while amplitudes are partially reproduced. It should be noted that there are discrepancies between the ultrasonic sensors and the image post-processing for the same instants.

The Fast Fourier Transform (FFT) has been applied to the experimental (ultrasonic) and numerical signals in order to identify the main frequencies involved in the movement; see Fig. 5. As expected, during the time periodic regime, the imposed frequency of 0.45 Hz and the corresponding multiples are present in both data sets. The magnitude of the amplitudes obtained at

each frequency, depends on the imposed amplitude of the tank motion. In the reported case, the imposed amplitude is enough to activate the harmonic frequencies in the free surface response. This fact is a measure of the disorder on the free surface induced by the tank geometry and the imposed tank motion. In the case that one of the activated frequencies coincides with a natural frequency of the tank, it can promote 3D effects. This fact was not found in the analyzed case. In addition, the first natural frequency was experimentally found in the range of $[0.47 - 0.5]$ Hz, and its value computed using linearized potential theory is 0.48 Hz using a two-dimensional model. In addition, many natural frequencies are analytically obtained within the range of those plotted in Fig. 5, i.e., lower than 5 Hz (see Table 1). In spite of that, no coincidences between such natural frequencies and the reported by the FFT analyses of the sensor signals were found. Nevertheless, some of the frequencies displayed in Fig. 5 are closer to natural frequencies of the system, this fact could justify the significant peaks reached at harmonics of the imposed frequency.

Mode	Frequency [Hz]	Mode	Frequency [Hz]	Mode	Frequency [Hz]
1	0.48	10	3.10	19	4.32
2	0.99	11	3.26	20	4.43
3	1.37	12	3.41	21	4.54
4	1.75	13	3.56	22	4.65
5	2.04	14	3.69	23	4.76
6	2.31	15	3.83	24	4.87
7	2.53	16	3.96	25	4.97
8	2.74	17	4.08		
9	2.92	18	4.20		

Table 1: Natural frequencies for the bottom stepped tank computed using linearized potential theory.

Figure 6 shows some snapshots of the experiment on the left for some instants of a period T, while the numerical results are shown in the right column for the same instants. There, the free surface patterns agree in each pair of images for every instant.

The pressure obtained numerically at some representative points is shown in Fig. 7 for the same time range as in Fig. 4. Taking as reference the level of the free surface at rest, the pressures in points P1 and P2 are plotted in Fig. 7(a). This figure shows a relatively low maximum amplitude, and

null pressures when the fluid level is lower than the reference, with higher peaks at the shallow side, P2, and alternate behavior of the gauges due to the imposed table movement. Fig. 7(b) to 7(d) shows the pressure evolution at the bottom of the tank. The pressure shown in Fig. 7 (b) at position of Sensor 1, is ranged from 350 to 630 Pa. In Figs. 7(c) and (d), at position of Sensors 2 and 3 respectively, pressure shows values from 850 to 1090 Pa, approximately. These pressure evolutions are consistent with the pressure determined from the instantaneous column of fluid (computed considering the Figs. 4). Such pressure is also plotted in Fig. 7(b) to 7(d) as a reference. Differences between pressures and such a reference could be understood as the dynamic effects induced by the motion.

Finally, the pressure fields for three instants of a table movement period T are represented in Fig. 8. Snapshots show the strong dependency of the pressure field on the fluid depth.

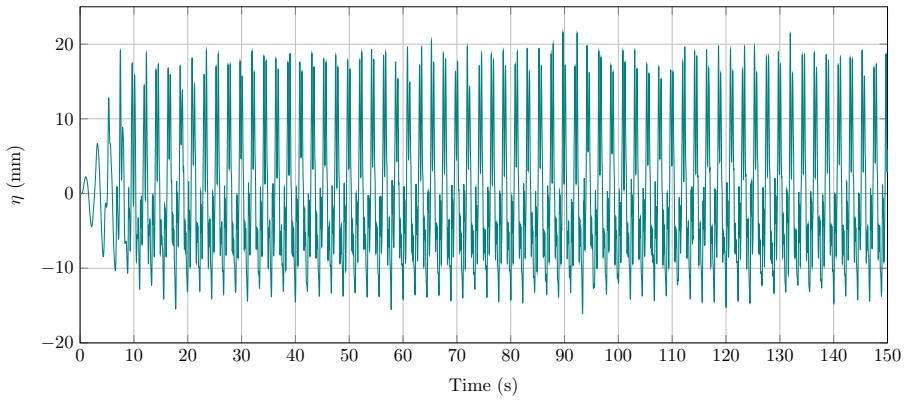

(a) Sensor 1

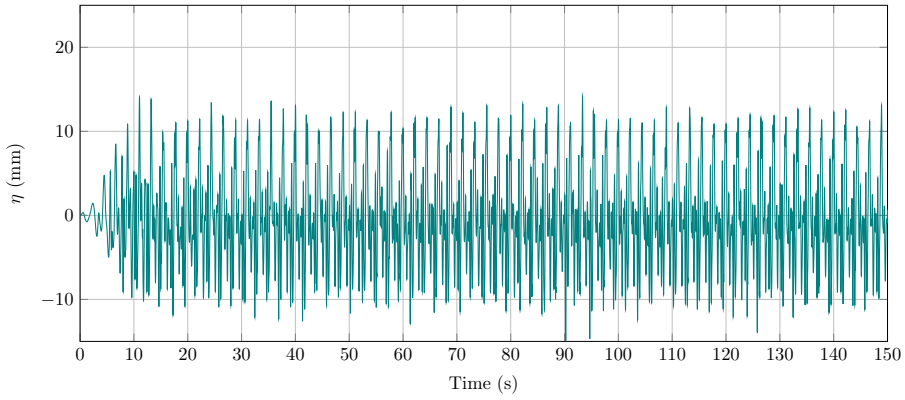

(b) Sensor 2

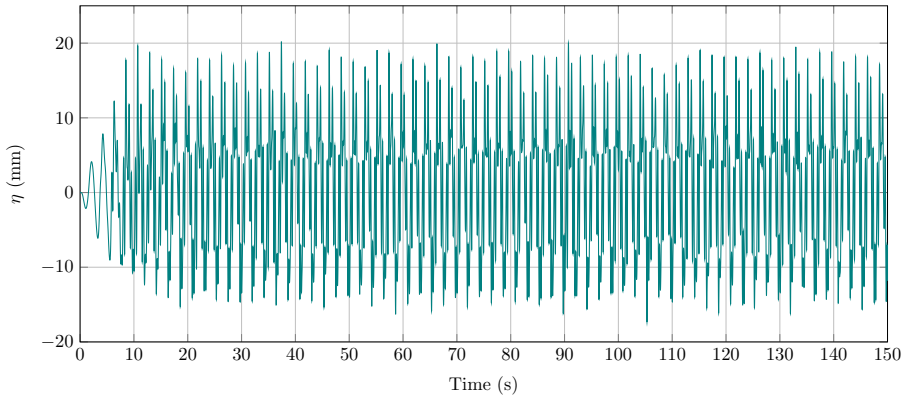

(c) Sensor 3

Figure 3: Numerical FS displacements η in the three reference positions.

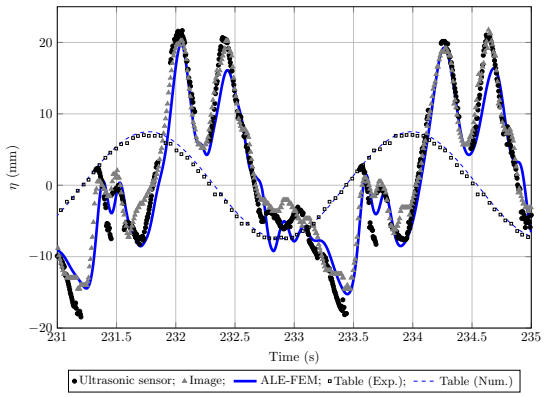

(a) Sensor 1

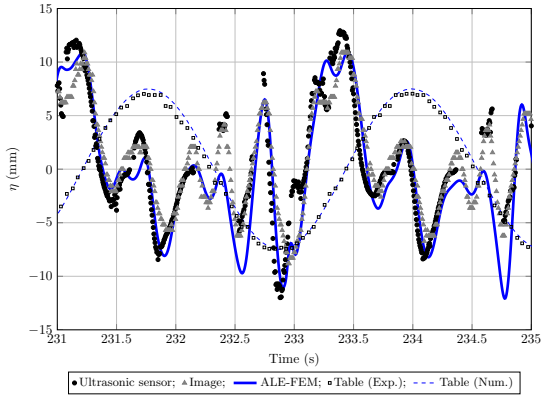

(b) Sensor 2

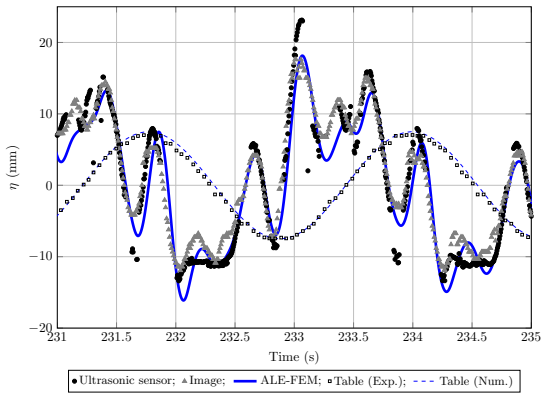

(c) Sensor 3

Figure 4: Free surface displacements: ultrasonic and image experimental measurements and numerical simulation. The shake table displacement experimentally measured and numerically imposed are also shown.

4. Sloshing in a rectangular-based tank

Two sloshing cases are formulated in an acrylic tank with a rectangular section of aspect ratio 2:1 placed over a shake table, as shown in Fig. 9(a). The tank width and depth are $L_1 = 0.388$ m and $L_2 = 0.183$ m, respectively, and the water level is $D = 0.10$ m. Four ultrasonic sensors A, B, C and D are placed as indicated in Fig. 9(b).

The water density is $\rho = 998.2$ kg m^{-3} and the dynamic viscosity is $\mu = 0.001$ kg (m s)$^{-1}$.

Boundary conditions for the NS problem are null velocities at the bottom of the tank ($\mathbf{u} = \mathbf{0}$) and perfect slip conditions on vertical walls ($\mathbf{u} \cdot \mathbf{n} = \mathbf{0}$.) Such conditions were satisfactorily applied and analysed in numerical solutions previously reported in [45] for 3D cases. This is given by the negligible effect of the boundary layer [13, 36], mostly due to its small thickness $y_l = \mathcal{O}(\sqrt{\nu/f})$, according to [47]. For the mesh dynamics, imposed displacements of the FS are given from the free surface solver, while the bottom nodes are fixed and the lateral walls are free to move over the corresponding planes.

The acceleration from gravity is $g = -9.81$ m s^{-2} in the x_3 direction, and the system is excited by a horizontal acceleration of amplitude 10 mm in the x_1 direction. Each example is excited at a different frequency, $f_1 = 1.28$ Hz in the quasi-2D sloshing of Sec. 4.1, and $f_2 = 2.10$ Hz in the near-resonance 3D sloshing of Sec. 4.2. Further information about the modes and the corresponding natural frequencies of this system can be found in the literature [20, 45].

4.1. Quasi-2D sloshing

The purpose of this example is to show the ability of the method to account for large amplitude displacements and sensitivity with respect to the coefficient C_{vol} in the volume-preserving stage. Furthermore, free surface displacements are contrasted with previously reported results [20].

The mesh-moving numerical results have been obtained with three different discretizations, each one characterized with a maximum h_{max}, a mean h_{mean}, and a refined h_{ref} mesh sizes, the last one in the neighborhood of the interface. The three meshes, composed by tetrahedral elements, have been created with the same rates $h_{\text{max}}/h_{\text{mean}} = 2$ and $h_{\text{mean}}/h_{\text{ref}} = 2$. Mesh 1 is composed of 1628 elements of mean element size $h_{\text{mean}} = 20$ mm, and is solved with a time step of $\Delta t_1 = 0.012$ s and $l_{\text{mix}} = 3.6$ mm. Mesh 2

is composed of 31825 elements of mean element size $h_{\text{mean}} = 10$ mm, and is solved with a time step of $\Delta t_2 = 0.006$ s and $l_{\text{mix}} = 1.8$ mm. Mesh 3 counts 113870 elements, with $h_{\text{mean}} = 5$ mm and is solved with a time step of $\Delta t_1 = 0.003$ s and $l_{\text{mix}} = 1$ mm. For the three cases, the volume-preserving parameters are the same, with $C_{\text{vol}} = 0.05$, and the cutoff viscosity is set in $\mu_{\text{max}} = 0.1$ kg (m s)$^{-1}$. Mixing length values have been adopted as $l_{\text{mix}} = C_{\text{t}} h_{\text{mean}}$, with $C_{\text{t}} \approx 0.18$.

The forced sloshing is applied from the beginning up to 120 s, when the horizontal acceleration is stopped, and then, the decay is registered up to a final time of 150 s. Figure 10 shows the free surface displacement η with respect to the configuration at rest for positions A and B in time, where three stages can be distinguished: initial transient, from 0 to 7 s; time-periodic, between 7 s and 120 s; and decay, from 120 s to the end of the simulation.

Some snapshots corresponding to near-maximum free surface displacements are shown in Fig. 11, where the nearly 2D behaviour of the case is apparent. The initial and deformed meshes are included in Fig. 12. The free surface ascends approximately 60% of the initial depth and descends up to 30%. Some low-amplitude ripples appear in the free surface near extreme laterals, where horizontal free surface velocities are very low, for meshes 2 and 3.

A comparison among experimental and different numerical results for this case is presented in Fig. 13 for control points A and B. The experimental results, wherein only confirmed measurements are reported, are well reproduced in phase; however, amplitudes are well compared only with meshes 2 and 3, and being the most refined mesh the one that provides the best approximation to the experimental results.

The mass-conserving stage is evaluated for the present example, solved with mesh 3. Comparing the results up to $t_c = 20$ s, the mass loss is 6.8% with $C_{\text{vol}} = 0$, while for $C_{\text{vol}} = 0.05$ it is 0.07%. For $C_{\text{vol}} = 0$, i.e., no volume control is applied, the mass loss reduces the depth of fluid in the domain from 100 mm to 93.2 mm, and the amplitude of the movement is also influenced (reduced) from the change in the conditions for the sloshing dynamics, as shown in Fig. 14. An alternative to reduce mass variations can be time and mesh refinement; however, the computing times significantly increase with such proposals.

Finally, Fig. 15 shows the velocity magnitude and direction for some instants of a period, corresponding to the maximum displacements to left and to right, the same as in Fig. 12, as well as an intermediate stage.

4.2. Near-resonance 3D sloshing

The sloshing case with $f_2 = 2.10$ Hz shows 3D behaviour both experimentally and numerically, associated with a $(1, 1)$ resonance mode of inviscid frequency $f = 2.12$ Hz, as described in the literature [45]. It should be noted that the 3D free surface movement is excited by a horizontal acceleration in the x_1 direction.

The problem is solved over a uniform mesh composed of 50877 tetrahedral elements of mean element size $h_2 = 6$ mm, with the same boundary conditions as in Sec. 4.1, time step $\Delta t = 0.01$ s, $l_{\text{mix}} = 0.8$ mm, $\mu_{\max} = 0.1$ kg (m s)$^{-1}$ and $C_{\text{vol}} = 0.05$. Initial conditions are null velocities and displacements. After a few periods of movement, a three-dimensional FS deformation is developed.

The numerical results are compared to experimental measurements of the FS displacements at the four sensor positions. Figure 16 shows the free surface displacements for two seconds from experimental and numerical measurements during the time periodic stage, where displacements η_A and η_C are coincident in phase, and η_B and η_D are in counter-phase with respect to the former. Therefore, the 3D behaviour of the system is verified. In both data sets, the amplitudes are less regular in the numerical solution, and negative amplitudes are more pronounced in the ALE solution. Nevertheless, the η_A measurements are less than η_C values, in magnitude, for both numerical and experimental results, and similarly for η_B and η_D.

Figure 17 represents the displacements at each probe at time t against the displacements at the same probe at time $t + T$ for 20 s in the time-periodic regime, where $T = f_2^{-1}$ is the period of the imposed movement. With these graphical data representations, the maximum elevations and falls of the movement are identified and the regularity of the phase is evaluated, showing that the points are located close to the $1 : 1$ diagonal.

An alternative representation consists of comparing the displacements at probe A with those at the rest of the probes, as shown in Fig. 18, where the dots represent the data from the time-periodic regime for 10 s. This representation is performed for the ALE results and the LS results obtained in [45]. Displacements η_A are compared to displacements η_B in Fig. 18 (top), showing the counter-phase of the movement at each position. In Fig. 18 (centre), dots are grouped close to the 1:1 diagonal, given that η_A and η_C show similar behaviour; i.e., because the movement is a (1,1) mode, the displacements at the A and C probes are in phase. Finally, the comparison between η_A and η_D in Fig. 18 (bottom) shows behaviour similar to that

in Fig. 18 (top); however, there is more dispersion, which is caused by the differences in amplitude of the movement of A and B with respect to C and D. Furthermore, using the time sequence in these graphs, the orbit and the corresponding sense of rotation are identified and sketched in dashed lines with the corresponding arrows. The LS results have been transformed, assuming a rotation of π in the x_3-coordinate for the position of the probes. The reason is because the mode (1,1) can be developed symmetrically with respect to the centre of the tank. In each corresponding diagram, the orbits turn in the same direction. As a particular case, the comparison of η_A and η_B of the top show a crossing in the orbit near the origin of the diagram. The experimental results lack registers for intermediate displacements, so there is no experimental confirmation of this particular behaviour.

The differences between displacements are plot in Fig. 19: $0.5(\eta_A-\eta_B)$ vs. $0.5(\eta_C-\eta_D)$ (top), $0.5(\eta_A-\eta_B)$ vs. $0.5(\eta_C-\eta_B)$ (middle), and $0.5(\eta_A-\eta_B)$ vs. $0.5(\eta_C-\eta_A)$ (bottom). The dots are represented with data from the time-periodic regime along 10 s, and the time sequence allows identifying an orbit in each diagram, representing the evolution of the movement inside the tank. With both numerical methods and with the probe location rotation aforementioned for the LS results, the orbits turns in the same direction.

The comparison among the two numerical results, ALE and LS, and the experimental measurements show satisfactory coincidences. The ALE displacements show more dispersion in the amplitudes, while the LS results are extremely regular and require an ad hoc initial condition to develop this special free surface oscillating mode. Unlike the LS strategy, which solves the water and the air phases, the present proposal models only the liquid part of the system, resulting in lower computational costs.

A FFT was performed for the experimental sensor registers in the time periodic regime, registering peaks at the imposed value of 2.1 Hz and others at 4.2 Hz, 6.3 Hz, and 8.4 Hz. The same analysis of the numerical results show the higher peak at 2.1 Hz, followed by 4.2 Hz, 6.3 Hz, and 8.4 Hz. In the last case, some lower peaks are registered in the range $[1.95, 2.0]$ Hz, which are associated to the natural frequencies of modes (0,1) or (2,0), which are 1.99 Hz and 1.93 Hz, respectively [45].

In Fig. 20, some snapshots of the experiment (left) are compared with the numerical results (right) during a period of excitation in the time-periodic stage. Some FS ripples also appear in the present example, both in the experimental and numerical FS.

The pressures computed under the sensor positions are plotted in Figs. 21

(a-d), together with the same parameter obtained with LS [45] for two oscillating periods of the table, represented with dashed thin lines. The pressure ranges registered are well compared with a reference pressure of 980 Pa at the bottom of the tank at rest. Pressure amplitudes obtained with the present model show slightly higher amplitudes than those obtained with LS, which is expected due to the higher free surface displacements obtained with ALE, as shown in Fig. 18. Particularly, under sensors C and D, there are two close peaks for each period in the ALE results, and a single peak in the case of LS. Here, as in [47] for a 2D-like sloshing, the double-peak can be explained as follows: first peak is due to a stagnation of the fluid when the table is reaching the end of the movement to $+x_1$ and the free surface rises on the left, e.g. under Sensor D at 110.4 s; then, there is a slight pressure drop; following, a new increase of pressure is registered when the tank is moving to the opposite side and the fluid drops on the left of the tank. A similar situation arises under Sensor C, that is placed at the opposed side of the tank with respect to Sensor D (see Fig. 9), when the shake table moves to the opposite side. Pressures under sensors A and B show a more pronounced double-peak in both of the numerical methods than in C and D. This is consistent with the free surface behavior: peaks of C and D take place close to the corresponding peaks in A and B, respectively.

5. Conclusions

A 3D strategy for one-phase fluid flow with a free surface, based on an arbitrary Lagrangian-Eulerian method, has been improved with the aim of solving long-term viscous sloshing problems with moderate displacements. The performance of the algorithm has been assessed through comparisons with experimental measurements and other numerical results.

The contributions of the work with respect to previous versions of the numerical method are the mass-conserving enforcement and the application of the three-dimensional strategy for mesh displacements based on minimal element distortion.

A horizontally excited bottom-stepped tank experimental study is introduced, where free surface displacements of water are measured by three probes using ultrasonic sensors and confirmed with image post-processing of the recorded experiences.

The mass-conserving strategy is tested for different values of the free parameter C_{vol}, showing that long time problems are not accurately reproduced

without the mass control. Furthermore, appropriate values for the correcting coefficient are given.

The CMD strategy shows robustness for moderate free surface displacements, including up to 60 % in positive displacements, as well as for small amplitude free surface perturbations, even dealing with tangled meshes.

The ability of the method to solve three-dimensional sloshing problems is shown for the 3D near-resonance case, where the three-dimensional mode is developed without any particular initial condition.

The free surface numerical results presented are all contrasted to experimental measurements, exhibiting good fits for all cases. The sloshing in a rectangular-based tank is also compared with other numerical methods, resulting in good agreement between strategies for the two frequencies analysed.

Acknowledgements

The authors appreciate the support provided by the following agencies and research projects: Chilean National Research and Development Agency (ANID) through FONDECYT grant 1210228; the Scientific Research Projects Management Department of the Vice Presidency of Research, Development and Innovation (DICYT-VRID, project 052016C) of the Universidad de Santiago de Chile; RED CYTED 516-RT0512 High Performance Computing in Engineering, Iberoamerican Scientific and Technological Development Program (CYTED, in Spanish); Argentinian Council for Scientific Research (CONICET) (grant PIP-2015-588); Argentinian Fund for Scientific Research and Technology (FONCyT) (grants PICT-2018-2920,PICT-2016-0640,PICT-2015-2904.PICT-2018-1607); Universidad Tecnológica Nacional (grant PID-4827), Universidad Nacional del Litoral (grants CAI+D 501-201101-00233, CAI+D 504-201501-00112-LI), and Universidad Nacional del Comahue (grant 04/I-251). The authors made extensive use of free software including GNU/Linux OS, GCC compilers, Octave, and open source software including ParaView.

[1] J. Wackers, B. Koren, H. Raven, A. Ploeg, A. Starke, G. Deng, P. Queutey, M. Visonneau, T. Hino, K. Ohashi, Free-surface viscous flow solution methods for ship hydrodynamics, Archives of Computational Methods in Engineering 18 (1) (2011) 1–41. doi:10.1007/s11831-011-9059-4.

[2] H. Yoshimura, I. Fujita, Investigation of free-surface dynamics in an open-channel flow, Journal of Hydraulic Research 58 (2) (2020) 231–247. doi:10.1080/00221686.2018.1561531.

[3] T.-W. Kang, H.-I. Yang, J.-S. Jeon, Earthquake-induced sloshing effects on the hydrodynamic pressure response of rigid cylindrical liquid storage tanks using CFD simulation, Engineering Structures 197 (2019) 109376. doi:10.1016/j.engstruct.2019.109376.

[4] H. Saghi, A. Hashemian, Multi-dimensional NURBS model for predicting maximum free surface oscillation in swaying rectangular storage tanks, Computers & Mathematics with Applications 76 (10) (2018) 2496 – 2513. doi:10.1016/j.camwa.2018.08.049.

[5] A. Kolaei, S. Rakheja, M. Richard, Three-dimensional dynamic liquid slosh in partially-filled horizontal tanks subject to simultaneous longitudinal and lateral excitations, European Journal of Mechanics - B/Fluids 53 (2015) 251 – 263. doi:10.1016/j.euromechflu.2015.06.001.

[6] O. M. Faltinsen, O. F. Rognebakke, A. N. Timokha, Classification of three-dimensional nonlinear sloshing in a square-base tank with finite depth, Journal of Fluids and Structures 20 (1) (2005) 81–103. doi:10.1016/j.jfluidstructs.2004.08.001.

[7] O. M. Faltinsen, O. F. Rognebakke, I. a. Lukovsky, A. N. Timokha, Multidimensional modal analysis of nonlinear sloshing in a rectangular tank with finite water depth, Journal of Fluid Mechanics 407 (2000) 201–234. doi:10.1017/S0022112099007569.

[8] O. M. Faltinsen, A. N. Timokha, A multimodal method for liquid sloshing in a two-dimensional circular tank, Journal of Fluid Mechanics 665 (2010) 457–479. doi:10.1017/S002211201000412X.

[9] N. Vaziri, M.-J. Chern, A. G. Borthwick, Effects of base aspect ratio on transient resonant fluid sloshing in a rectangular tank: A numerical study, Ocean Engineering 105 (2015) 112–124. doi:10.1016/j.oceaneng.2015.06.020.

[10] S. Elgeti, H. Sauerland, Deforming fluid domains within the finite element method: Five mesh-based tracking methods in comparison,

Archives of Computational Methods in Engineering 23 (2) (2016) 323–361. doi:10.1007/s11831-015-9143-2.

[11] C. W. Hirt, B. D. Nichols, Volume of fluid (VOF) method for the dynamics of free boundaries, Journal of Computational Physics 39 (1) (1981) 201–225. doi:10.1016/0021-9991(81)90145-5.

[12] R. Löhner, C. Yang, E. Oñate, On the simulation of flows with violent free surface motion, Computer Methods in Applied Mechanics and Engineering 195 (41–43) (2006) 5597–5620. doi:10.1016/j.cma.2005.11.010.

[13] H. Akyildız, N. E. Ünal, Sloshing in a three-dimensional rectangular tank: numerical simulation and experimental validation, Ocean Engineering 33 (16) (2006) 2135–2149. doi:10.1016/j.oceaneng.2005.11.001.

[14] O. Oxtoby, A. Malan, J. Heyns, A computationally efficient 3D finite-volume scheme for violent liquid–gas sloshing, International Journal for Numerical Methods in Fluids 79 (6) (2015) 306–321. doi:10.1002/fld.4055.

[15] M.-J. Li, Interaction between free surface flow and moving bodies with a dynamic mesh and interface geometric reconstruction approach, Computers & Mathematics with Applications (2020). doi:10.1016/j.camwa.2020.01.020.

[16] M. Sussman, P. Smereka, Axisymmetric free boundary problems, Journal of Fluid Mechanics 341 (1997) 269–294. doi:10.1017/S0022112097005570.

[17] P. Frey, D. Kazerani, T. Ta, An adaptive numerical scheme for solving incompressible 2-phase and free-surface flows, International Journal for Numerical Methods in Fluids 87 (11) (2018) 543–582. doi:10.1002/fld.4502.

[18] R. F. Ausas, G. C. Buscaglia, S. R. Idelsohn, A new enrichment space for the treatment of discontinuous pressures in multi-fluid flows, International Journal for Numerical Methods in Fluids 70 (7) (2012) 829–850. doi:10.1002/fld.2713.

[19] A. Huerta, W. K. Liu, Viscous flow with large free surface motion, Computer Methods in Applied Mechanics and Engineering 69 (3) (1988) 277–324. doi:10.1016/0045-7825(88)90044-8.

[20] M. A. Cruchaga, R. S. Reinoso, M. A. Storti, D. J. Celentano, T. E. Tezduyar, Finite element computation and experimental validation of sloshing in rectangular tanks, Computational Mechanics 52 (6) (2013) 1301–1312. doi:10.1007/s00466-013-0877-0.

[21] T. E. Tezduyar, Finite elements in fluids: Stabilized formulations and moving boundaries and interfaces, Computers & Fluids 36 (2) (2007) 191 – 206. doi:10.1016/j.compfluid.2005.02.011.

[22] C.-H. Wu, B.-F. Chen, T.-K. Hung, Hydrodynamic forces induced by transient sloshing in a 3D rectangular tank due to oblique horizontal excitation, Computers & Mathematics with Applications 65 (8) (2013) 1163–1186. doi:10.1016/j.camwa.2013.02.012.

[23] A. Rafiee, F. Pistani, K. Thiagarajan, Study of liquid sloshing: numerical and experimental approach, Computational Mechanics 47 (1) (2011) 65–75. doi:10.1007/s00466-010-0529-6.

[24] J. R. Shao, H. Q. Li, G. R. Liu, M. B. Liu, An improved sph method for modeling liquid sloshing dynamics, Comput. Struct. 100–101 (2012) 18—-26. doi:10.1016/j.compstruc.2012.02.005.

[25] B. Bouscasse, M. Antuono, A. Colagrossi, C. Lugni, Numerical and experimental investigation of nonlinear shallow water sloshing, International Journal of Nonlinear Sciences and Numerical Simulation 14 (2) (2013) 123–138. doi:10.1515/ijnsns-2012-0100.

[26] M. D. Green, J. Peiró, Long duration sph simulations of sloshing in tanks with a low fill ratio and high stretching, Computers & Fluids 174 (2018) 179–199. doi:10.1016/j.compfluid.2018.07.006.

[27] J. M. Gimenez, L. M. González, An extended validation of the last generation of particle finite element method for free surface flows, Journal of Computational Physics 284 (2015) 186–205. doi:10.1016/j.jcp.2014.12.025.

[28] M. Sussman, E. G. Puckett, A coupled level set and volume-of-fluid method for computing 3D and axisymmetric incompressible two-phase flows, Journal of Computational Physics 162 (2) (2000) 301–337. doi:10.1006/jcph.2000.6537.

[29] D. Liu, W. Tang, J. Wang, H. Xue, K. Wang, Comparison of laminar model, RANS, LES and VLES for simulation of liquid sloshing, Applied Ocean Research 59 (2016) 638 – 649. doi:10.1016/j.apor.2016.07.012.

[30] D. Enright, F. Losasso, R. Fedkiw, A fast and accurate semi-Lagrangian particle level set method, Computers & Structures 83 (6–7) (2005) 479–490. doi:10.1016/j.compstruc.2004.04.024.

[31] V. Le Chenadec, H. Pitsch, A 3D unsplit forward/backward volume-of-fluid approach and coupling to the level set method, Journal of Computational Physics 233 (1) (2013) 10–33. doi:10.1016/j.jcp.2012.07.019.

[32] S. Shin, D. Juric, A hybrid interface method for three-dimensional multiphase flows based on front tracking and level set techniques, International Journal for Numerical Methods in Fluids 60 (7) (2009) 753–778. doi:10.1002/fld.1912.

[33] M. Cruchaga, L. Battaglia, M. Storti, J. D'Elía, Numerical modeling and experimental validation of free surface flow problems, Archives of Computational Methods in Engineering 23 (1) (2016) 139–169. doi:10.1007/s11831-014-9138-4.

[34] T. J. R. Hughes, W. K. Liu, T. K. Zimmermann, Lagrangian-Eulerian finite element formulation for incompressible viscous flows, Computer Methods in Applied Mechanics and Engineering 29 (3) (1981) 329–349. doi:10.1016/0045-7825(81)90049-9.

[35] L. Charlot, S. Etienne, A. Hay, D. Pelletier, A. Garon, High-order time integrators for front-tracking finite-element analysis of viscous free-surface flows, International Journal for Numerical Methods in Fluids 77 (11) (2015) 668–693. doi:10.1002/fld.4001.

[36] T. Yong, Y. Baozeng, Simulation of large-amplitude three-dimensional liquid sloshing in spherical tanks, AIAA Journal 55 (6) (2017) 2052–2059. doi:10.2514/1.J055798.

[37] A. Charin, Z. Tuković, H. Jasak, L. Silva, P. Lage, A moving mesh interface tracking method for simulation of liquid–liquid systems, Journal of Computational Physics 334 (2017) 419 – 441. doi:10.1016/j.jcp.2017.01.011.

[38] E. L. Grotle, H. Bihs, V. Æsøy, Experimental and numerical investigation of sloshing under roll excitation at shallow liquid depths, Ocean Engineering 138 (Supplement C) (2017) 73 – 85. doi:10.1016/j.oceaneng.2017.04.021.

[39] L. Battaglia, J. D'Elía, M. A. Storti, N. M. Nigro, Numerical simulation of transient free surface flows using a moving mesh technique, ASME Journal of Applied Mechanics 73 (6) (2006) 1017–1025. doi:10.1115/1.2198246.

[40] E. J. López, N. M. Nigro, M. A. Storti, J. A. Toth, A minimal element distortion strategy for computational mesh dynamics, International Journal for Numerical Methods in Engineering 69 (9) (2007) 1898–1929.

[41] PETSc-FEM, A general purpose, parallel, multi-physics FEM program, https://cimec.org.ar/petscfem, GNU General Public License (GPL) (2020). doi:10.5281/zenodo.3700857.

[42] MPI, Message Passing Interface, https://www.mpi-forum.org/docs/ (2020).

[43] S. Balay, S. Abhyankar, M. F. Adams, J. Brown, P. Brune, K. Buschelman, L. Dalcin, A. Dener, V. Eijkhout, W. D. Gropp, D. Karpeyev, D. Kaushik, M. G. Knepley, D. A. May, L. C. McInnes, R. T. Mills, T. Munson, K. Rupp, P. Sanan, B. F. Smith, S. Zampini, H. Zhang, H. Zhang, PETSc users manual, Tech. Rep. ANL-95/11 - Revision 3.11, Argonne National Laboratory (2019).
URL `https://www.mcs.anl.gov/petsc`

[44] P. Sagaut, Large Eddy Simulation for Incompressible Flows: An Introduction, Scientific Computation, Springer, 2005.

[45] L. Battaglia, M. Cruchaga, M. Storti, J. D'Elía, J. Nuñez Aedo, R. Reinoso, Numerical modelling of 3D sloshing experiments in rect-

angular tanks, Applied Mathematical Modelling 59 (2018) 357–378. doi:10.1016/j.apm.2018.01.033.

[46] C. Argyropoulos, N. Markatos, Recent advances on the numerical modelling of turbulent flows, Applied Mathematical Modelling 39 (2) (2015) 693 – 732. doi:10.1016/j.apm.2014.07.001.

[47] X. Jin, P. Lin, Viscous effects on liquid sloshing under external excitations, Ocean Engineering 171 (2019) 695–707. doi:10.1016/j.oceaneng.2018.10.024.

[48] A. Brooks, T. J. R. Hughes, Streamline upwind/Petrov-Galerkin formulations for convection dominated flows with particular emphasis on the incompressible Navier-Stokes equations, Computer Methods in Applied Mechanics Engineering 32 (1-3) (1982) 199–259. doi:10.1016/0045-7825(82)90071-8.

[49] T. E. Tezduyar, S. Mittal, S. E. Ray, R. Shih, Incompressible flow computations with stabilized bilinear and linear-equal-order interpolation velocity-pressure elements, Computer Methods in Applied Mechanics and Engineering 95 (2) (1992) 221–242. doi:10.1016/0045-7825(92)90141-6.

[50] R. F. Ausas, E. A. Dari, G. C. Buscaglia, A geometric mass-preserving redistancing scheme for the level set function, International Journal for Numerical Methods in Fluids 65 (8) (2011) 989–1010. doi:10.1002/fld.2227.

[51] M. Cruchaga, D. Celentano, P. Breitkopf, P. Villon, A. Rassineux, A surface remeshing technique for a Lagrangian description of 3D two-fluid flow problems, International Journal for Numerical Methods in Fluids 63 (4) (2010) 415–430. doi:10.1002/fld.2073.

[52] H. Saito, L. E. Scriven, Study of coating flow by the finite element method, Journal of Computational Physics 42 (1) (1981) 53–76. doi:10.1016/0021-9991(81)90232-1.

[53] M. Behr, F. Abraham, Free surface flow simulations in the presence of inclined walls, Computer Methods in Applied Mechanics and Engineering 191 (47-48) (2002) 5467–5483.

[54] A. Castorrini, A. Corsini, F. Rispoli, K. Takizawa, T. E. Tezduyar, A stabilized ALE method for computational fluid–structure interaction analysis of passive morphing in turbomachinery, Mathematical Models and Methods in Applied Sciences 29 (05) (2019) 967–994. doi:10.1142/S0218202519410057.

[55] E. J. López, N. M. Nigro, M. A. Storti, Simultaneous untangling and smoothing of moving grids, International Journal for Numerical Methods in Engineering 76 (7) (2008) 994–1019. doi:10.1002/nme.2347.

[56] E. Castillo, M. A. Cruchaga, J. Baiges, J. Flores, An oil sloshing study: adaptive fixed-mesh ALE analysis and comparison with experiments, Computational Mechanics 63 (5) (2019) 985–998.

[57] E. Zamora, L. Battaglia, M. Storti, M. Cruchaga, R. Ortega, Numerical and experimental study of the motion of a sphere in a communicating vessel system subject to sloshing, Physics of Fluids 31 (8) (2019) 087106.

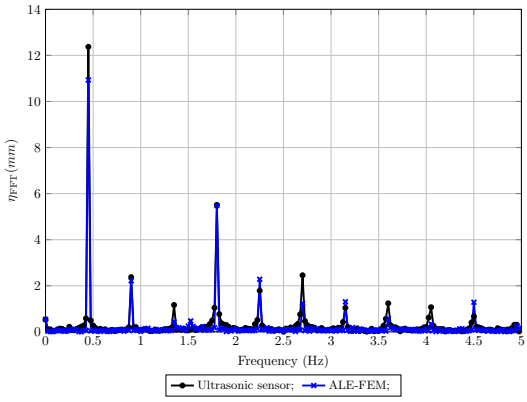

(a) Sensor 1

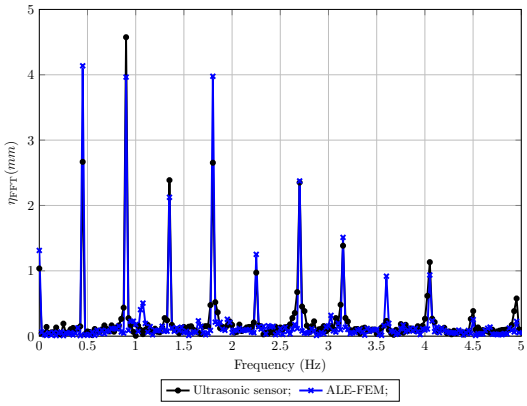

(b) Sensor 2

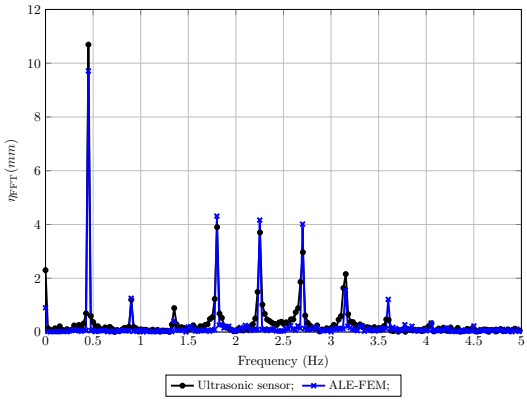

(c) Sensor 3

Figure 5: Comparison of experimental and numerical frequencies from FFT of sensor signals.

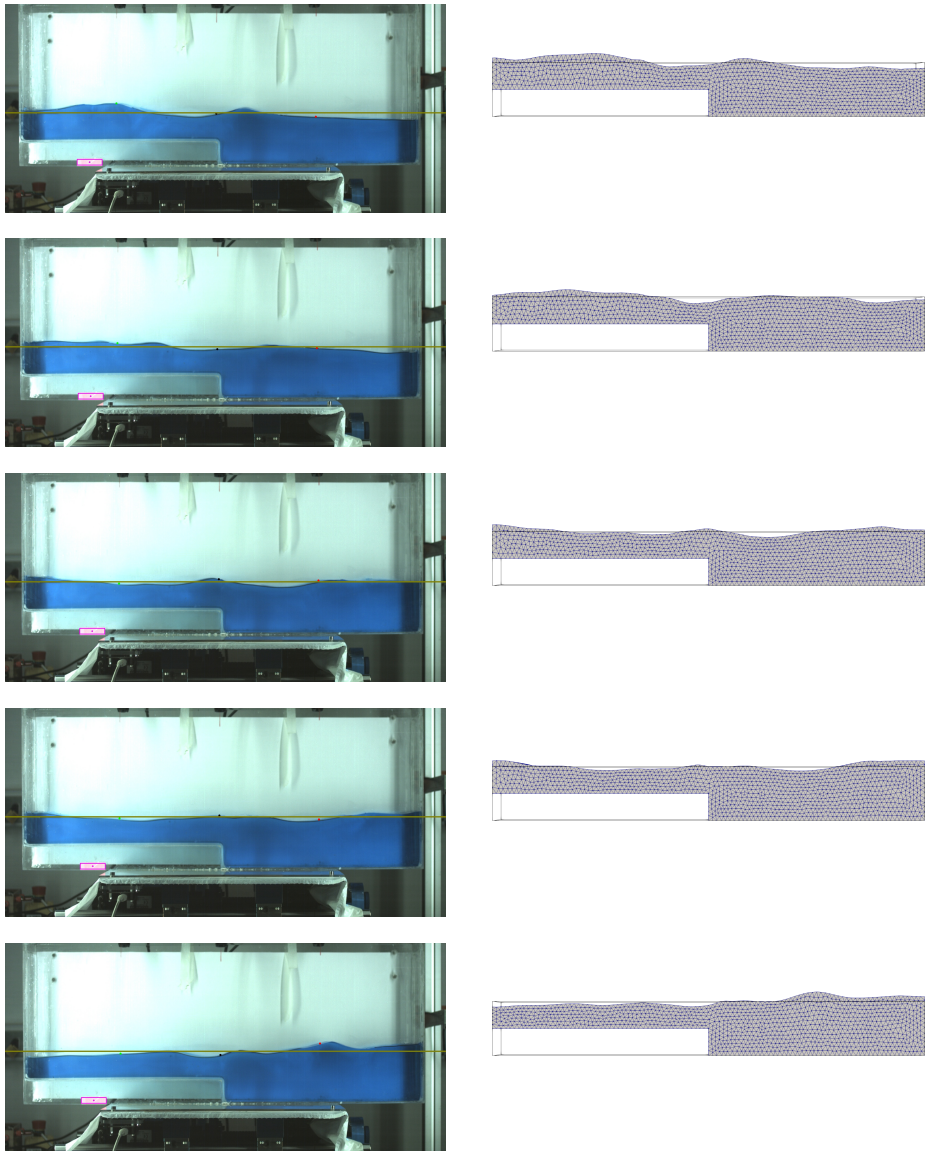

Figure 6: Comparison of experimental (left) and numerical (right) shapes for the free surface for some instants of a period T. From top to bottom: $0.250T$, $0.300T$, $0.375T$, $0.400T$, and $0.500T$.

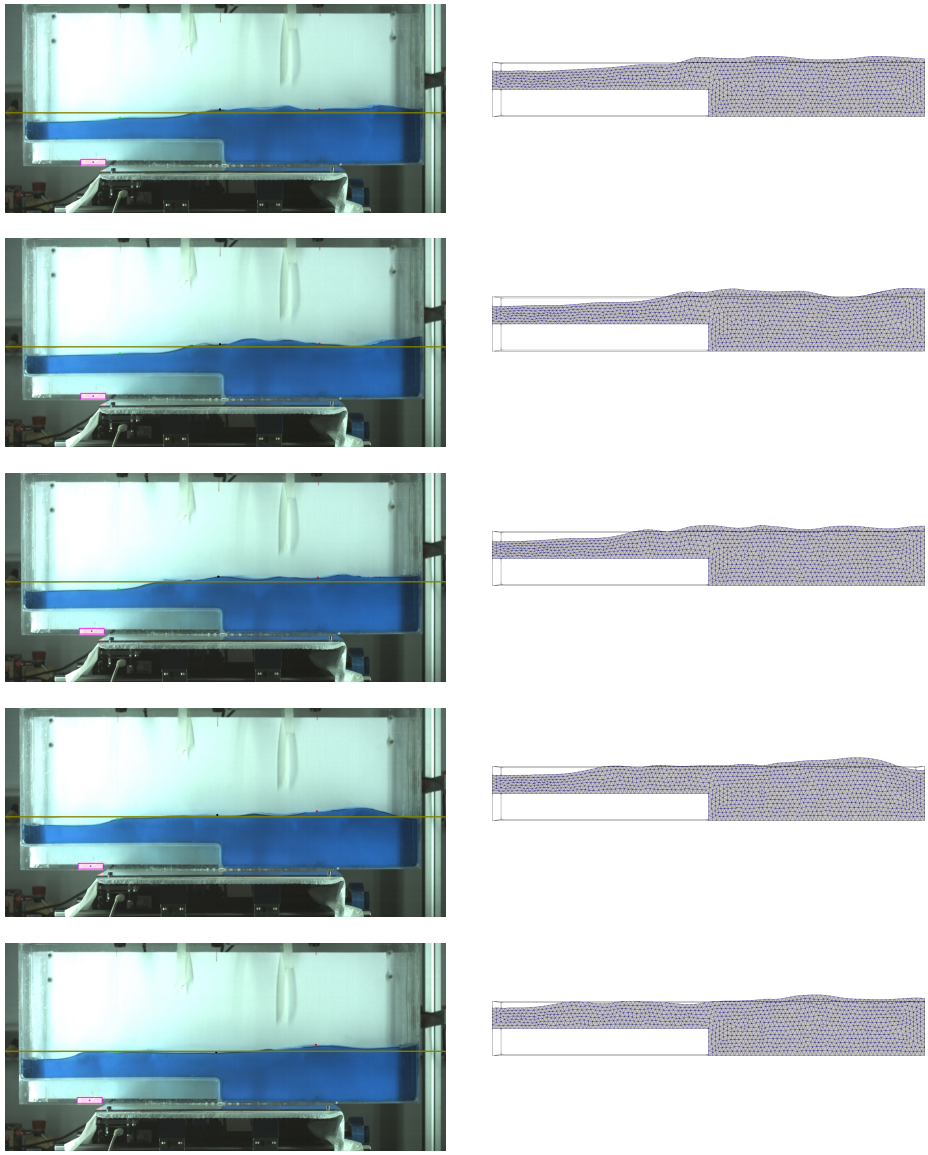

Figure 6 (Cont.): Comparison of experimental (left) and numerical (right) shapes for the free surface for some instants of a period T. From top to bottom: $0.600T$, $0.625T$, $0.700T$, $0.750T$, and $0.800T$.

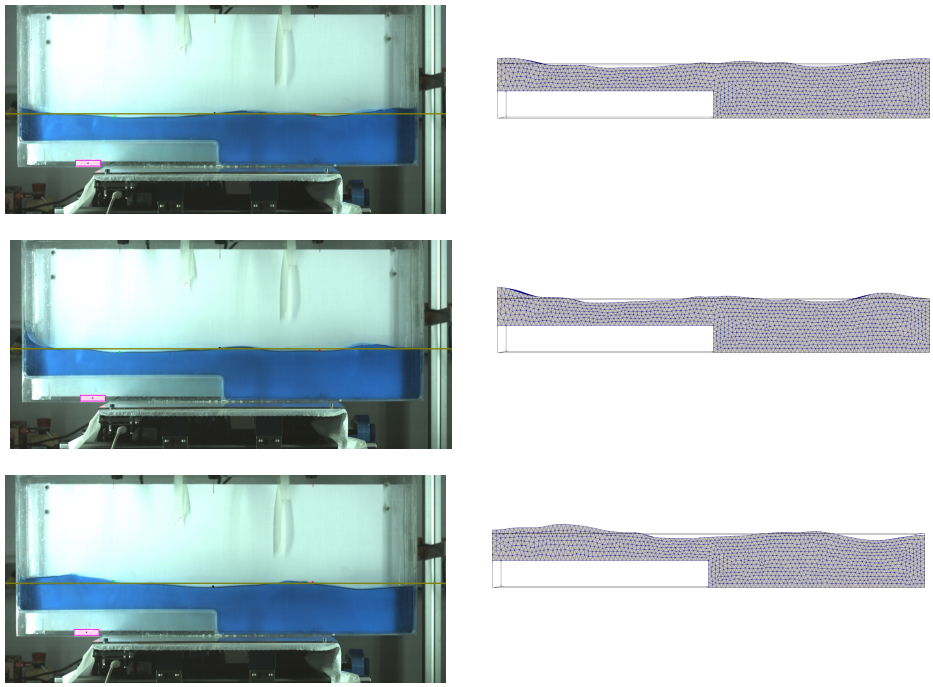

Figure 6 (Cont.): Comparison of experimental (left) and numerical (right) shapes for the free surface for some instants of a period T. From top to bottom: $0.875T$, $0.900T$, and T.

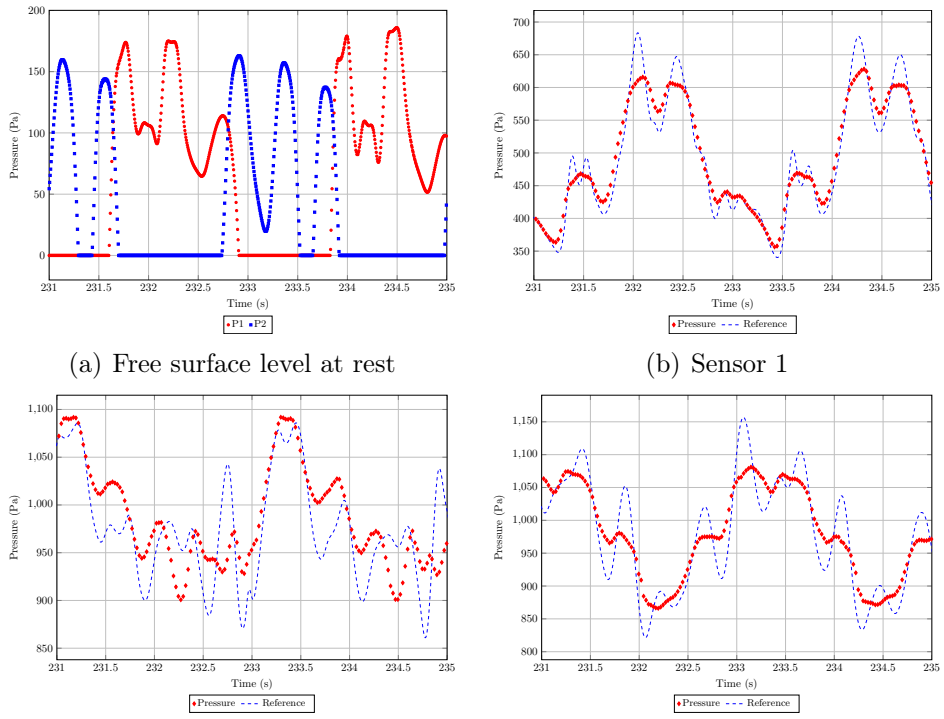

(a) Free surface level at rest

(b) Sensor 1

(c) Sensor 2

(d) Sensor 3

Figure 7: Pressure numerically obtained: (a) at points $P1$ and $P2$ (see Fig. 2 (a)) considering the level of the free surface at rest as reference; (b) to (d) at the bottom of the tank at positions of sensors 1 to 3, respectively.

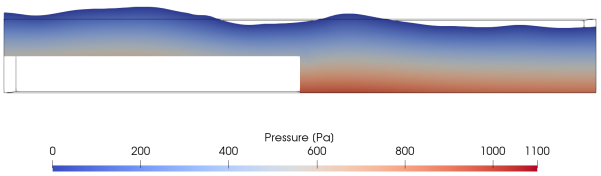

(a) $0.250T$

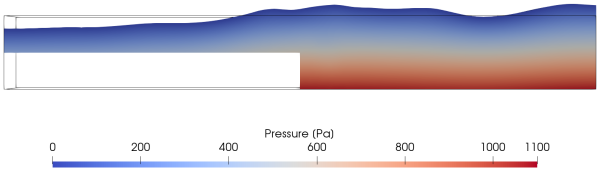

(b) $0.625T$

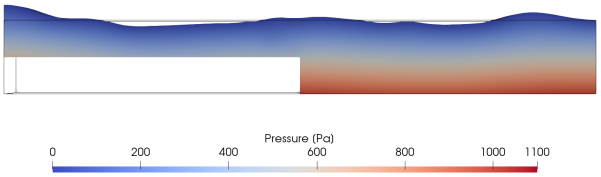

(c) $0.900T$

Figure 8: Pressure fields for some instants of a period T.

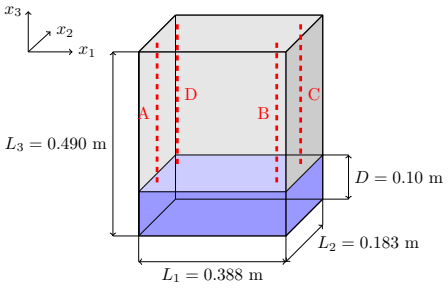

(a)

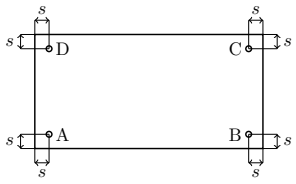

(b)

Figure 9: Tank dimensions (a) and sensor positions (b), with $s = 25$ mm, error ± 1 mm.

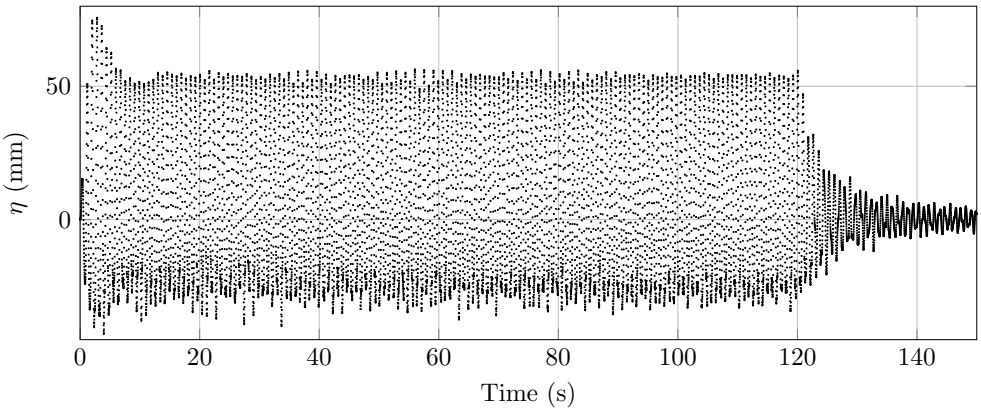

(a) Control point A

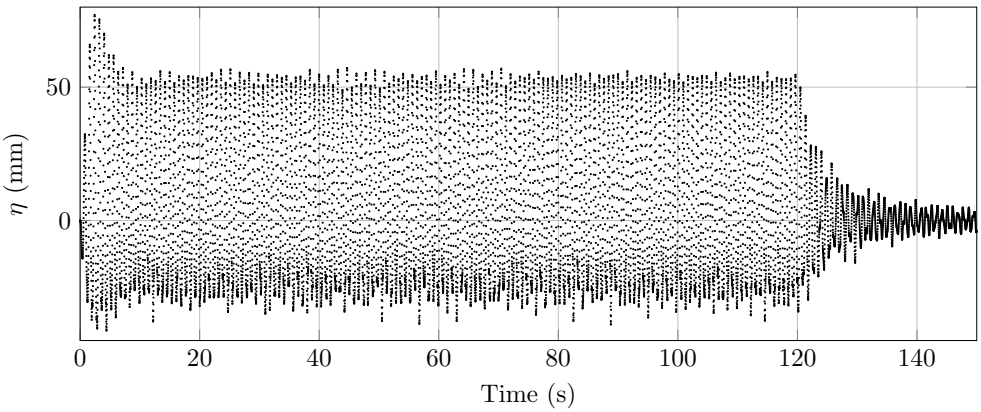

(b) Control point B

Figure 10: Free surface displacements obtained for $f_1 = 1.28$ Hz with mesh 2.

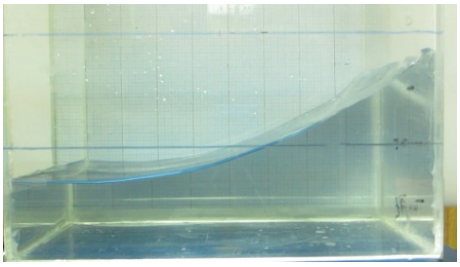

(a) Maximum free surface displacement to right, experimental

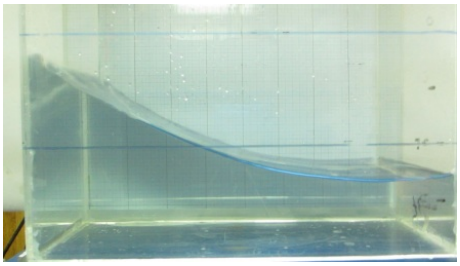

(b) Maximum free surface displacement to left, experimental

Figure 11: Maximum displacements in stationary regime for $f_1 = 1.28$ Hz. Lateral view.

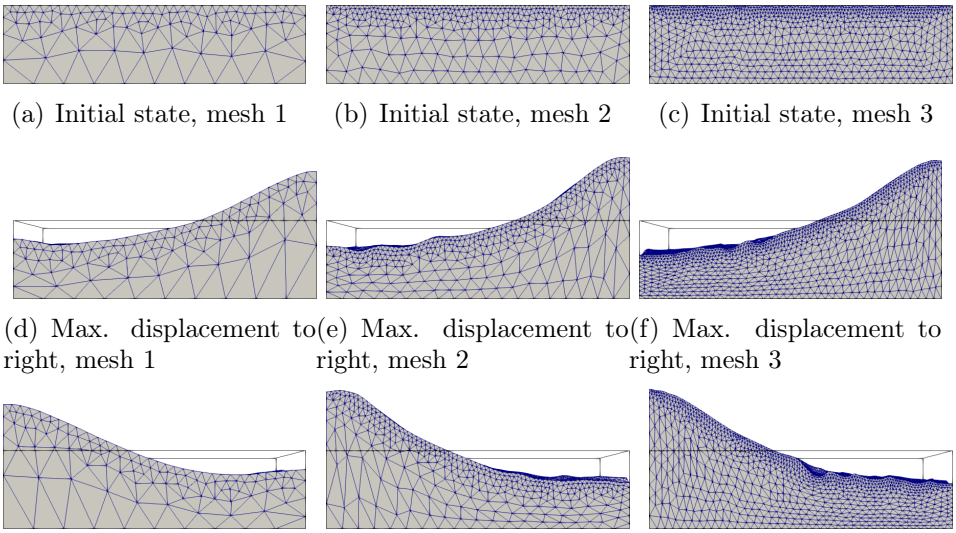

(a) Initial state, mesh 1 (b) Initial state, mesh 2 (c) Initial state, mesh 3

(d) Max. displacement to right, mesh 1 (e) Max. displacement to right, mesh 2 (f) Max. displacement to right, mesh 3

(g) Max. displacement to left, mesh 1 (h) Max. displacement to left, mesh 2 (i) Max. displacement to left, mesh 3

Figure 12: Initial and deformed domain for maximum free surface displacements for $f_1 = 1.28$ Hz. Lateral view for the three meshes.

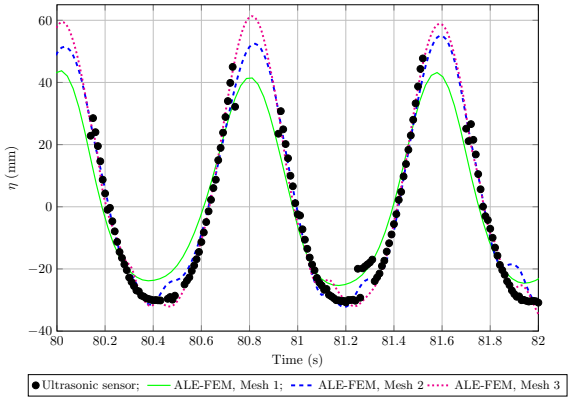

(a) Control point A

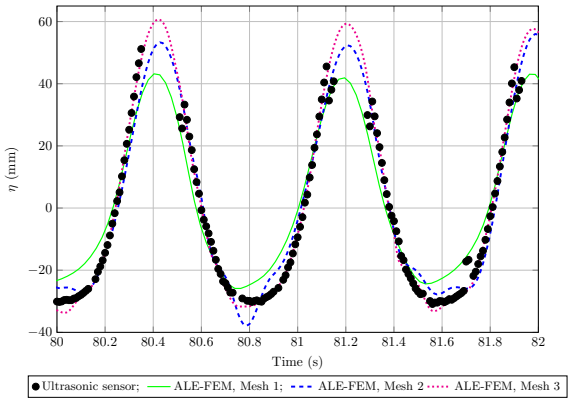

(b) Control point B

Figure 13: Comparison between ultrasonic register and the three ALE meshes, for control points A and B in the quasi-2D sloshing with $f_1 = 1.28$ Hz.

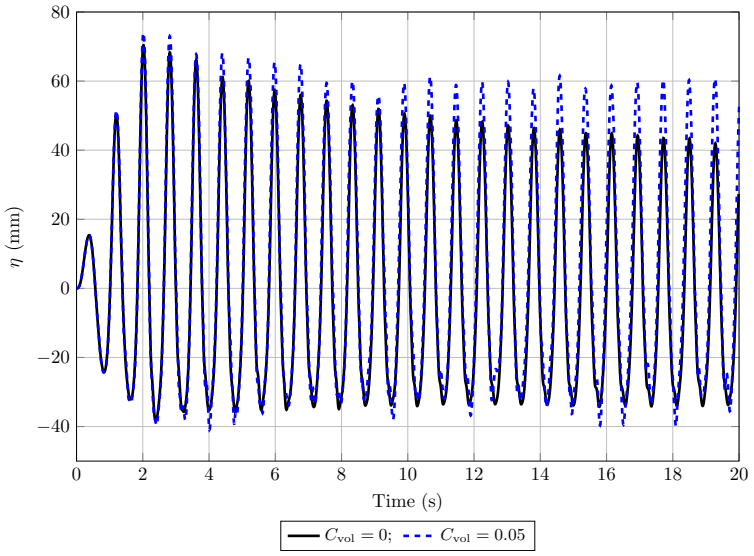

Figure 14: Free surface displacement η measured at control point A for mesh 3 with and without the mass-conserving effect.

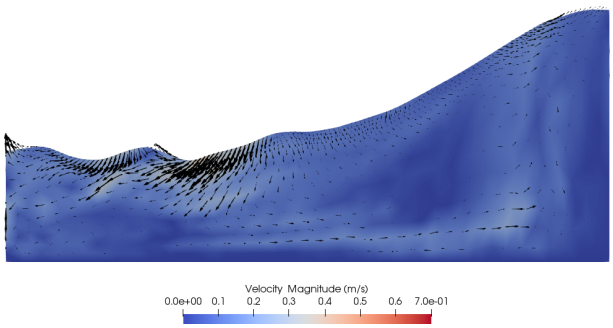

(a) $t = 13.40$ s

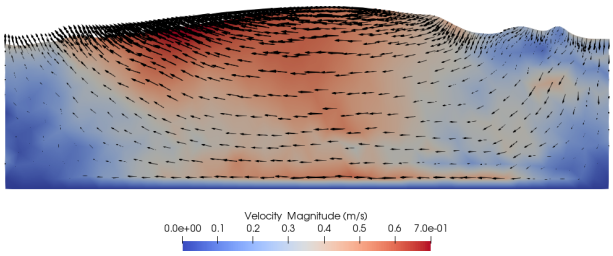

(b) $t = 13.60$ s

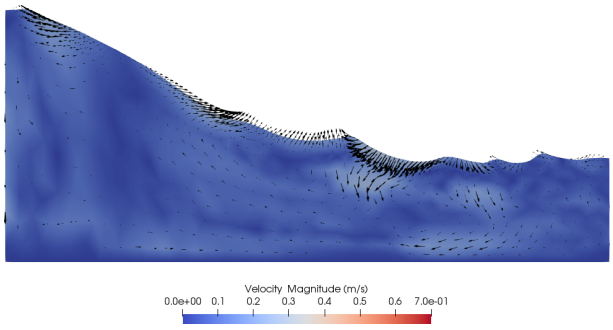

(c) $t = 13.79$ s

Figure 15: Velocity magnitude and direction in time periodic regime for some time steps in the case with $f_1 = 1.28$ Hz and mesh 3, $y = 0.183$ m.

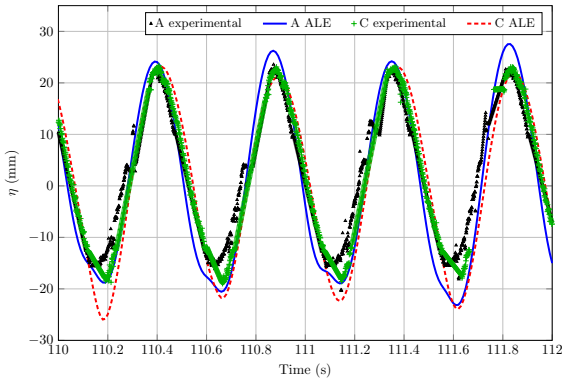

(a) Sensors A and C

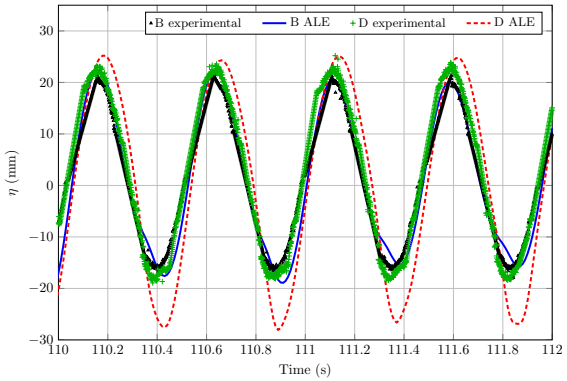

(b) Sensors B and D

Figure 16: Free surface displacements during 2 s for $f_2 = 2.1$ Hz. Experimental measurements (dots) and numerical results (lines).

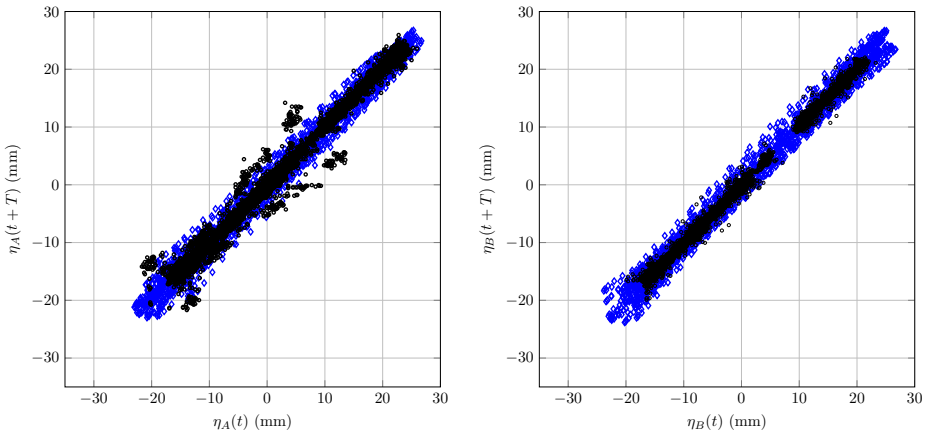

(a) Sensor A (b) Sensor B

(c) Sensor C (d) Sensor D

Figure 17: Free surface displacements comparison: $\eta(t)$ vs. $\eta(t+T)$ along 20 s, for $f_2 = 2.1$ Hz. The diamonds are the ALE results and the circles are experimental measurements.

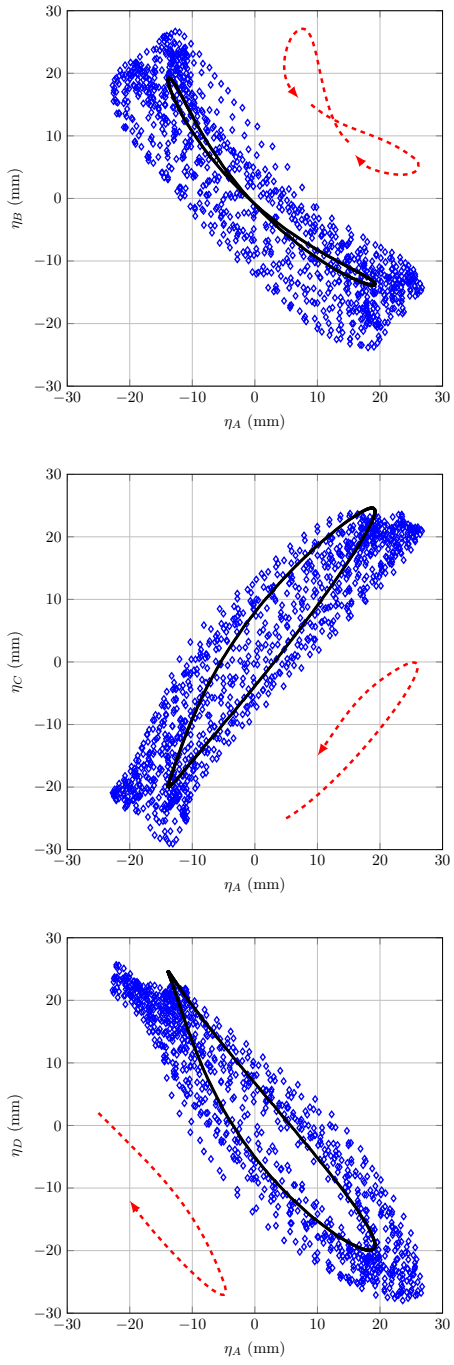

Figure 18: Displacements η_A vs. η_B (top), η_C (middle) and η_D (bottom), during 5 s for $f = 2.1$ Hz in the time periodic regime. Diamonds are the ALE results, while black symbols have been obtained with LS [45]. Dashed lines with arrows sketch the time sequence of the orbits.

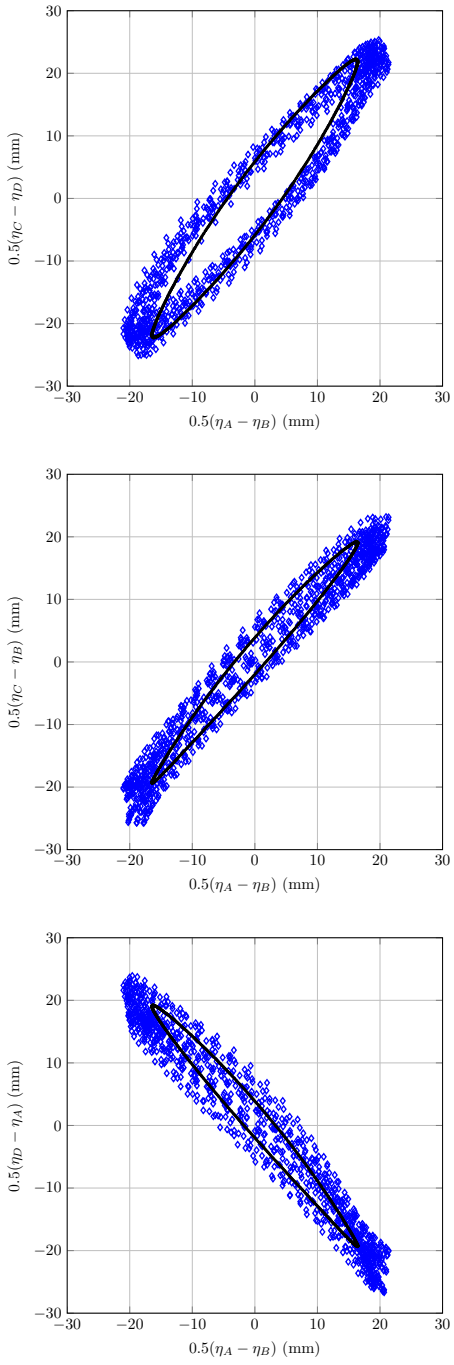

Figure 19: Displacements analysis: $0.5(\eta_A - \eta_B)$ vs. $0.5(\eta_C - \eta_D)$ (top), $0.5(\eta_A - \eta_B)$ vs. $0.5(\eta_C - \eta_B)$ (middle), $0.5(\eta_A - \eta_B)$ vs. $0.5(\eta_D - \eta_A)$ (bottom), along 20 s, for $f_2 = 2.1$ Hz. Diamonds are the ALE results, while black symbols have been obtained with LS [45].

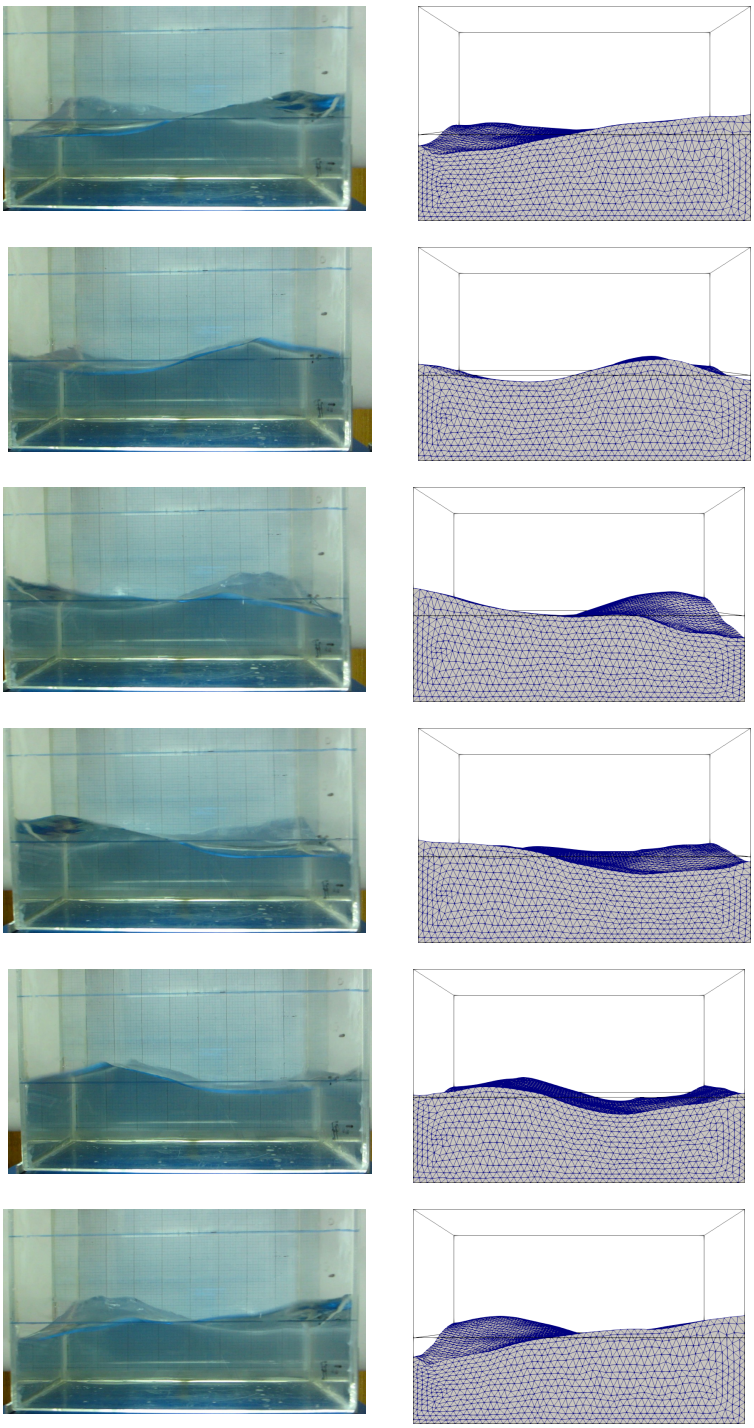

Figure 20: Comparison of experimental (left) and numerical (right) shapes for the free surface at some instants of a period T for $f_4 = 2.10$ Hz.

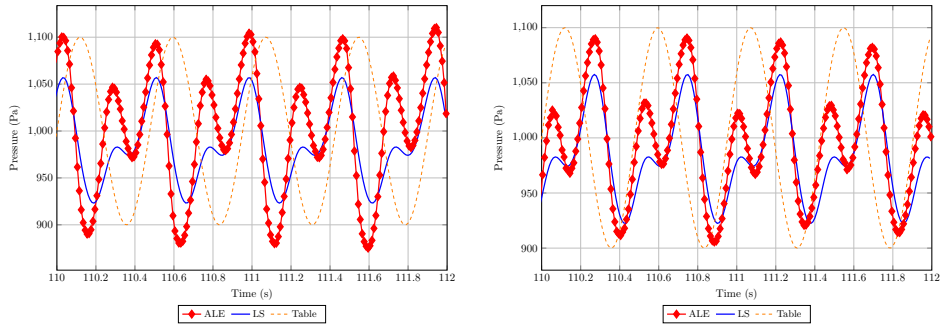

(a) Under Sensor A

(b) Under Sensor B

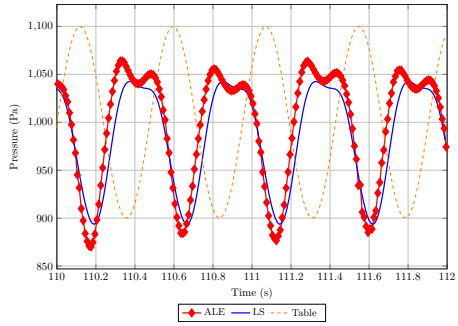

(c) Under Sensor C

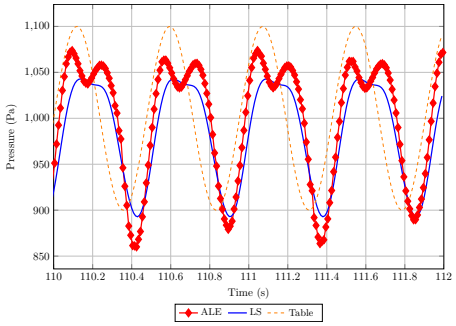

(d) Under Sensor D

Figure 21: Pressure numerically obtained at the bottom of the rectangular tank, under sensor positions A-D (see references in Fig. 9 (a)). The table displacements are represented out of scale, with dashed lines.